ELSEVIER

PII: S0309-1708(98)00040-2

Advances in Water Resources Vol. 22, No. 6, pp 577–584, 1999

0309-1708/99/$ – see front matter

Determination of phase-volume fractions from tomographic measurements in two-phase systems

V. Clausnitzer & J. W. Hopmans*

University of California, Department of Land, Air and Water Resources, Hydrology Program, Veihmeyer Hall, Davis, CA 95616, USA

(Received 13 April 1998; revised 20 September 1998; accepted 5 October 1998)

A method is proposed to determine the phase-volume fractions in tomographic representations of two-phase systems. The method is applicable in cases where no independent mean values for the phase-characteristic property (α) are available, such as in standard X-ray computed tomography (CT) using a polychromatic source. The proposed procedure is based on fitting a sum of three parametric expressions to the histogram of α-values. The terms include two normal probability-density functions to account for noisy pure-phase values, and an analytical expression to account for intermediate values due to interface-containing voxels and blurring. To test the method, it was applied to several X-ray CT data sets of two-phase systems with known volume fractions and varying α-ranges, including a system with only about one standard deviation difference between the mean phase α-values, i.e., with substantial overlap between the noisy pure-phase distributions. The accuracy for the considered cases was found to be approximately 2 vol% or better. As an example, the proposed fitting procedure was used to determine the representative elementary volume needed for porosity estimation of a porous medium consisting of 0.5-mm glass beads.

1 INTRODUCTION

Tomographic methods provide nondestructive cross-sectional or three-dimensional object representations in terms of a phase-characteristic property, such as electrical capacitance or electrical resistance; absorption, diffraction, or reflection of light; or emission of electromagnetic radiation from nuclei in response to external magnetic fields (nuclear magnetic resonance)[5]. In radiation-based (gamma or X-ray) computed tomography (CT), which will be considered here, this property is the specific attenuation of electromagnetic radiation and depends on local atomic composition and density within the object. Typically, the spatial resolution is between 0.01 and 10 mm. Computed tomography has been successfully used to investigate the spatial distribution of soil bulk density[8] and soil-water content[1,8,9], and to determine the porosity of rock cores[11]. In addition, tomographic techniques have been applied to study miscible displacement in porous media[6,14], and multiphase flow[15], including recent application to real-time monitoring[5].

A specific class of problems involves tomographic data sets (or subsets) of spatial domains containing exactly two phases. Examples include the investigation of spatial variation of porosity in porous media, or the measurement of gas bubbles in a liquid[7]. To determine the phase-volume fractions for such data, the mean values for the phase-characteristic property must be known for each phase. These values can be theoretically predicted only under certain conditions. For example, in the case of radiation-based CT the atomic composition and density of both phases must be known and the radiation must be monochromatic. This paper describes a method to identify the local phase-volume fractions for all cases where independent mean values are not available or not easily obtained, such as in standard X-ray tomography using a polychromatic source.

* Corresponding author. jwhopmans@ucdavis.edu

2 THEORY

The subsequent analysis assumes the following preconditions:

- The spatial domain of interest, D, contains two immiscible phases (e.g., solid and fluid). Volumetric phase content is denoted by θ_A and θ_B for phases A and B, respectively, with $\theta_A + \theta_B = 1$.
- A set of n nonoverlapping, equal-sized volume elements or voxels completely fills D.
- There exists a property α with distinct values α_A and α_B ($\alpha_A < \alpha_B$) for phases A and B, respectively. In radiation-based CT, α represents the linear attenuation coefficient with units of inverse length.
- A value α_i has been obtained for each voxel i. The complete set of n measured α-values is denoted by $\boldsymbol{\alpha}$.

2.1 Voxel categories and volume fractions

If $\boldsymbol{\alpha}$ were free of any noise and artifacts, an individual value α_i would belong to one of three subsets: $\boldsymbol{A}$, pure phase A ($\alpha_i = \alpha_A$); $\boldsymbol{B}$, pure phase B ($\alpha_i = \alpha_B$); or $\boldsymbol{M}$, intermediate values ($\alpha_A < \alpha_i < \alpha_B$). Intermediate α-values occur for all voxels that contain a phase interface. In addition, due to blurring, the spatial range of intermediate α-values usually extends over several voxels in the direction normal to the interface orientation. The degree of blurring in $\boldsymbol{\alpha}$ depends on the sharpness of the individual projections, i.e., on geometric factors such as size of X-ray source and detectors. Denoting the number of α-values in each subset by N_A, N_B, and N_M, respectively, three volume fractions can be defined as

$$\phi_k \equiv \frac{N_k}{n} \quad k = \mathrm{A}, \mathrm{B}, \mathrm{M} \tag{1}$$

with $\sum \phi_k = 1$. The expected value for $\boldsymbol{\alpha}$ is given by

$$E(\boldsymbol{\alpha}) = \phi_A E(\boldsymbol{A}) + \phi_B E(\boldsymbol{B}) + \phi_M E(\boldsymbol{M}), \tag{2}$$

with

$$E(\boldsymbol{A}) = \alpha_A \quad \text{and} \quad E(\boldsymbol{B}) = \alpha_B. \tag{3}$$

The α-value for a voxel containing an interface is assumed to follow from linear interpolation between α_A and α_B according to the fractioning of the voxel volume between phases A and B. This is an approximation inasmuch as a nonlinear interpolation may be implied, for example, by the partial-volume effect' in radiation-based CT. This effect is related to the orientation of phase interfaces relative to the beam direction for each projection within a scanning sequence. The theoretical average α-value based on the volume fractions for the phases present within the voxel is a maximum value, which represents the effective α-value only if beam and interface are normal to each other. For all other alignments, the effective α-value is smaller, causing a theoretical bias toward α_A in the measured α-values for all voxels containing an interface. The effect is trivial if α_i^{-1} is much larger than the voxel size[10]. The significance of the error due to linear interpolation thus depends on the particular tomographic method used, but is in all cases limited by ϕ_M.

The fraction ϕ_M contains volume contributions from phases A and B, $\phi_{M,A}$ and $\phi_{M,B}$, respectively, with $\phi_M = \phi_{M,A} + \phi_{M,B}$. If all intermediate values are due to interface-containing voxels only (no blurring), the expected value for $\boldsymbol{M}$ is given as

$$E(\boldsymbol{M}) = \frac{\phi_{M,A}}{\phi_M}\alpha_A + \frac{\phi_{M,B}}{\phi_M}\alpha_B \tag{4}$$

based on linear interpolation for each voxel. We will assume that eqn (4) holds for $\boldsymbol{\alpha}$ subject to blurring as well, i.e., that the blurring is unbiased and does not affect $E(\boldsymbol{M})$. As a consequence, we require that the boundaries of D do not coincide to any significant degree with a phase interface. Since volumetric phase content values are given by

$$\theta_k = \phi_k + \phi_{M,k}, \quad k = \mathrm{A},\ \mathrm{B}, \tag{5}$$

it follows, after substituting (3) and (4) into (2), that

$$\theta_A = \frac{\alpha_B - E(\boldsymbol{\alpha})}{\alpha_B - \alpha_A} \quad \text{and} \quad \theta_B = \frac{E(\boldsymbol{\alpha}) - \alpha_A}{\alpha_B - \alpha_A}. \tag{6}$$

Consequently, θ_A and θ_B can be computed once $E(\boldsymbol{\alpha})$, α_A, and α_B have been obtained. The value of $E(\boldsymbol{\alpha})$ is easily calculated as

$$E(\boldsymbol{\alpha}) = \frac{1}{n}\sum_{i=1}^{n}\alpha_i. \tag{7}$$

For polychromatic radiation, the parameters α_A and α_B cannot generally be predicted independently, but are effective values depending on phase distribution and beam energy spectrum. If the difference between α_A and α_B is sufficiently large, relative to the noise, to prevent significant overlap between the probability-density functions (PDF) of α-values in $\boldsymbol{A}$ and $\boldsymbol{B}$, both parameters may be estimated as the peak locations in the $\boldsymbol{\alpha}$-histogram. If this is not the case, a statistically sufficient number of voxels known with high certainty to represent only one phase (i.e., from locations sufficiently far from phase interfaces to not be affected by blurring) may be possible to identify, and a mean effective α-value be estimated for the respective phase. As a faster and more generally applicable alternative, we propose to obtain α_A and α_B directly from the histogram of all measured α-values by fitting a parametric model PDF.

2.2 Development of model PDF

First, $\boldsymbol{\alpha}$ is assumed to be free of noise. The probability-density functions for the two distributions of pure-phase α-values are then given by

$$f_k^*(\alpha) \equiv \delta(\alpha - \alpha_k), \quad k = \mathrm{A},\ \mathrm{B},$$

where $\delta(\alpha)$ is the Dirac delta function. The distribution of the intermediate α-values is not necessarily symmetric,

but can be skewed towards either α_A or α_B, depending on the geometry of the phase interfaces within the voxel set. To describe the probability-density function f_M^* of this generally unknown distribution, an expression is needed that is flexible, simple and has few parameters. We propose the following definition, which has the desired properties:

$$f_M^*(\alpha) \equiv \begin{cases} \dfrac{(\alpha-\alpha_A)^{\gamma_A}(\alpha_B-\alpha)^{\gamma_B}}{\int_{\alpha_A}^{\alpha_B}(\alpha-\alpha_A)^{\gamma_A}(\alpha_B-\alpha)^{\gamma_B}\,d\alpha}, & \alpha_A \leqslant \alpha \leqslant \alpha_B, \\ 0, & \alpha < \alpha_A,\ \alpha_B < \alpha. \end{cases} \tag{8}$$

The integral in the denominator ensures that

$$\int_{-\infty}^{\infty} f_M^*\, d\alpha = 1,$$

while the two parameters γ_A and $\gamma_B (\gamma_A \gamma_B > 0)$ allow for a wide range of shapes for the distribution function. Several examples are shown in Fig. 1 using the normalized variable ξ that maps the interval $[\alpha_A, \alpha_B]$ to [0, 1]. Note that switching γ_A and γ_B is equivalent to a horizontal mirroring of the curve.

In general, $\boldsymbol{\alpha}$ is not free of noise due to the random nature of both photon emission and attenuation. Note that this randomness is unrelated to any randomness in the spatial distribution of A and B. To include noise in $\boldsymbol{\alpha}$, we will assume that it is Gaussian[10], with a variance independent of α[13]. Gaussian noise acts as a convolution kernel G on the probability-density functions for the respective distributions of α-values in all three categories. Due to symmetry, G does not affect $E(\boldsymbol{A})$, $E(\boldsymbol{B})$, and $E(\boldsymbol{M})$, so that eqn (6) remain valid in the presence of noise. Convolution of each f_k^* (k = A, B, M) with the Gaussian kernel G of standard deviation σ,

$$f_k(\alpha) \equiv (f_k^* * G) = \int_{-\infty}^{\infty} f_k^*(\alpha') G(\alpha' - \alpha) d\alpha', \quad k = \mathrm{A},\ \mathrm{B},\ \mathrm{M} \tag{9}$$

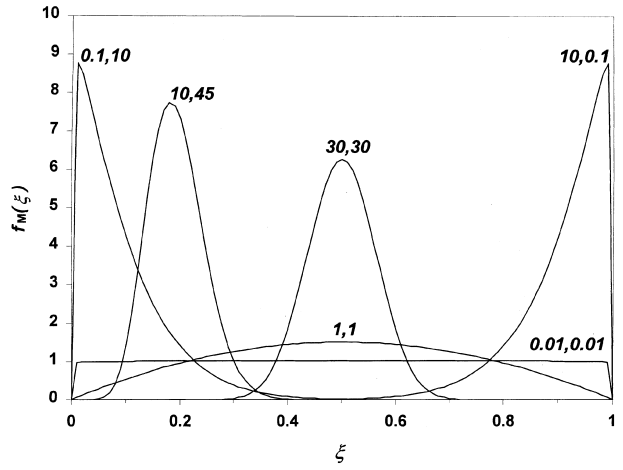

Fig. 1. Behavior of f_M^* plotted for the dummy variable ξ. Number pairs indicate values for γ_A and γ_B for the respective curve.

results in respective probability-density functions for $\boldsymbol{A}$ and $\boldsymbol{B}$,

$$f_k(\alpha) = \frac{1}{\sigma\sqrt{2\pi}} \exp\left[\frac{-(\alpha-\alpha_k)^2}{2\sigma^2}\right], \quad k = \mathrm{A},\ \mathrm{B}$$

Some spreading of $\boldsymbol{A}$ and $\boldsymbol{B}$ is also due to 'beam-hardening' in the case of polychromatic radiation. This phenomenon is related to the relatively stronger attenuation of the lower end of the X-ray energy spectrum and causes α-values of voxels near the object center to be artificially lowered relative to those near the circumference, with a smooth transition in between. The degree of beam-hardening depends on X-ray source spectrum and object attenuation. A portion of this additional spreading will appear as noise and thus be included in eqn (9). The remaining portion will be considered insignificant relative to $\phi_A f_A$ and $\phi_B f_B$. The convolution $f_M^* * G$ to obtain f_M is computed numerically, with the limits of integration, $-\infty$ and ∞, replaced by $\alpha_A - 4\sigma$ and $\alpha_B + 4\sigma$, respectively. The complete model for the PDF of the α-distribution is given by

$$f(\alpha) = \phi_A f_A(\alpha) + \phi_B f_B(\alpha) + \phi_M f_M(\alpha). \tag{10}$$

Definitions (1), (8), and (9) ensure that

$$\int_{-\infty}^{\infty} f\, d\alpha = 1.$$

2.3 Procedure

Seven independent parameters, ϕ_A, ϕ_B, α_A, α_B, σ, γ_A, and γ_B, are included in eqn (10) (note that $\phi_M = 1 - \phi_A - \phi_B$). The following procedure can be used to estimate these parameters:

1. Compute $E(\boldsymbol{\alpha})$ using eqn (7).
2. From the measured $\boldsymbol{\alpha}$, compute a normalized histogram $\hat{f}(\alpha)$ such that
$$\sum_{j=1}^{m} \hat{f}_j \Delta\alpha = 1,$$
where $\Delta\alpha$ and m denote class size and total number of classes, respectively, and j is the class index (class value α_j increases with j).
3. Provide initial estimates for ϕ_A, ϕ_B, α_A, α_B, and σ from inspection of $\hat{f}(\alpha)$. If there is sufficient separation between the pure-phase distributions, α_A and α_B can be estimated as the peak center locations, while ϕ_A and ϕ_B should correspond to the relative area under each peak.
4. Provide initial guesses for γ_A and γ_B.
5. Fit $f(\alpha)$ to $\hat{f}(\alpha)$.
6. Compute θ_A and θ_B using eqn (6).

The parameter optimization (step 5) was implemented using the Levenberg–Marquardt-based LM-OPT code[4]. The software is written in C and available from the authors upon request. The large number of parameters makes the fitting procedure susceptible to premature

termination due to local optima (nonuniqueness). Thus the optimization should be repeated with several sets of initial parameter values to increase the likelihood of identifying the global optimum. For example, approximately 10 parameter sets were tried for each of the applications discussed in the next section. An alternative function for cases where n is too small to obtain a meaningful histogram is given in Appendix A.

Note that for systems containing three or more phases, the individual contributions of each phase to the fraction of mixed voxels, ϕ_M, cannot be determined from a fitted model PDF and ϕ_M must effectively be treated as an additional phase[10]. Therefore, the procedure described here is limited to two-phase systems.

3 APPLICATION AND DISCUSSION

3.1 Tests using capillary tubes

A rectangular domain of $1.547 \times 1.547 \times 1.617$ mm^3 was considered. The domain consisted of $88 \times 88 \times 92$ cubic voxels with a side length of 18.4 μm, resulting in a total number of voxels, n, of 712,448. Voxel values $\boldsymbol{\alpha}$ represent specific X-ray attenuation and were obtained in a CT scan of a vertical glass capillary tube. A microfocus cone-beam scanner equipped with a polychromatic *Leitz* source (Tungsten anode) was used at Scientific Measurement Systems, Austin, TX. Source potential and current were 125 keV and 0.1 mA, respectively, resulting in a 10-μm source spot size. The scanned portion of the tube was horizontally centered in the domain. The two phases present were (A) air and (B) glass. Independent values of 0.82 and 1.50 mm for the inner and outer tube diameter, respectively, were determined using a scanning electron microscope. These measurements imply a theoretical volumetric phase content value θ_A of 0.527. Using eqn (7), a value of 0.02433 mm^{-1} was obtained for $E(\boldsymbol{\alpha})$. A normalized histogram was $\hat{f}(\alpha)$ was computed with m equal to 100. Initial estimates for ϕ_A, ϕ_B, α_A, α_B, and σ were obtained from inspection of $\hat{f}(\alpha)$. Fig. 2 shows the optimized $f(\alpha)$, its three components, and $\hat{f}(\alpha)$. Dotted lines denote $\phi_A f_A$ (left peak) and $\phi_B f_B$ (right peak). The thin and thick solid lines represent $\phi_M f_M$ and f, respectively, and the individual data points denote $\hat{f}$. Initial and fitted parameter values are given in Table 1, together with θ_A computed from fitted parameters using eqn (6). Goodness of fit is expressed as root-mean-square rms, given by

$$\text{rms} = \left(\frac{1}{m} \sum_{j=1}^{m} [\hat{f}_j - f(\alpha_j)]^2 \right)^{0.5}$$

The computed θ_A-value of 0.522 differs only by 0.5 vol% from the theoretical value of 0.527. In contrast, had α_A and α_B been obtained by identifying 100 pure-phase voxels for each phase and averaging their respective α-values, θ_A-values as low as 0.482 and as high as 0.620 could have been obtained, depending on the location of the selected voxels.

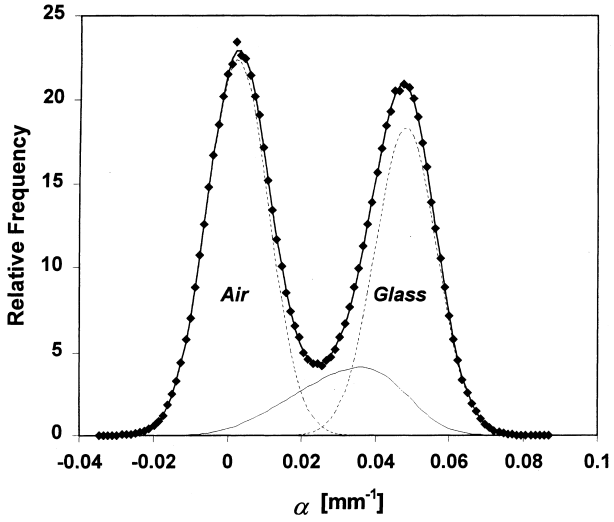

Fig. 2. Comparison of $\hat{f}$ and f for glass/air test case. Dotted lines denote $\phi_A f_A$ (left peak) and $\phi_B f_B$ (right peak). The thin and thick solid lines represent $\phi_M f_M$ and f, respectively, and the individual points denote $\hat{f}$.

Table 1. Comparison of initial and optimized parameters for capillary-tube data

Parameter	Initial estimate	Final estimate
ϕ_A	0.4	0.4686
ϕ_B	0.4	0.3838
α_A [mm^{-1}]	0.0	0.00256
α_B [mm^{-1}]	0.05	0.04815
σ [mm^{-1}]	0.01	0.00836
γ_A	1.0	0.8746
γ_B	1.0	0.0531
rms	–	0.114
ϕ_M	–	0.1476
$E(\boldsymbol{\alpha})$ [mm^{-1}]	–	0.02433
θ_A	–	**0.522**

A, air; B, glass. The theoretical θ_A-value was 0.527.

The phase interfaces in the data set (i.e., the vertical inner and outer tube surfaces) were found to be blurred over approximately three voxel lengths in the normal direction. Thus the number of voxels containing the physical interface area (36,128) was multiplied by three and divided by n to obtain a theoretical value of 0.152 for the fraction of voxels with intermediate α-values (ϕ_M). The optimized ϕ_M-value was 0.148.

Subsequently, we tested the accuracy for different fluid/glass systems with decreasing separation distance between α_A and α_B. Similar capillary tubes as in the previous example were filled with air, water, and three different concentrations (20, 40, and 60 g/l) of sodium-iodide (NaI) solution (fluid phase, A) and

simultaneously scanned. Voxel dimensions were again $(18.4\ \mu m)^3$. To limit the number of phases in each domain to two, the vertical domain boundary was defined as a cylinder with a 70-voxel (1.288-mm) diameter, and thus located within the respective capillary tube (glass phase, B), excluding any outside air. Only complete voxels were included, resulting in a horizontal domain cross-section of 3853 voxels (1.304 mm^2). Domain height was 31 voxels (0.570 mm), resulting in a total domain size of 0.744 mm^3 with n equal to 119,443. The theoretical value for the volumetric fluid content was 0.405 based on geometric considerations.

The values of all optimized parameters are shown, together with rms, ϕ_M, $E(\boldsymbol{\alpha})$, and θ_A, in Table 2. No meaningful result could be obtained for the 60-g/l NaI solution because in this case the values of α_A and α_B differed by less than 0.075 σ, which prevented a distinction between solution and glass phases. Fig. 3

Table 2. Optimized parameter values for different fluids in capillary tubes

Fluid	Air	Water	NaI solution [g/l]	
			20	40
ϕ_A	0.3708	0.3737	0.3846	0.3835
ϕ_B	0.5378	0.5685	0.5829	0.6165
α_A [mm^{-1}]	0.00345	0.01832	0.02937	0.03938
α_B [mm^{-1}]	0.04836	0.04885	0.04913	0.04968
σ [mm^{-1}]	0.00812	0.00784	0.00794	0.00802
γ_A	5.8238	4.0889	1.6325	– [a]
γ_B	2.8094	3.8857	0.0599	– [a]
rms	0.231	0.294	0.344	0.334
ϕ_M	0.0914	0.0578	0.0325	0 [a]
$E(\alpha)$	0.03022	0.03660	0.04136	0.04573
θ_A	**0.404**	**0.401**	**0.393**	**0.384**

A, fluid; B, glass. The theoretical θ_A-value was 0.405.
[a] ϕ_M was fixed at zero by forcing $(\phi_A + \phi_B) = 1$ during the optimization.

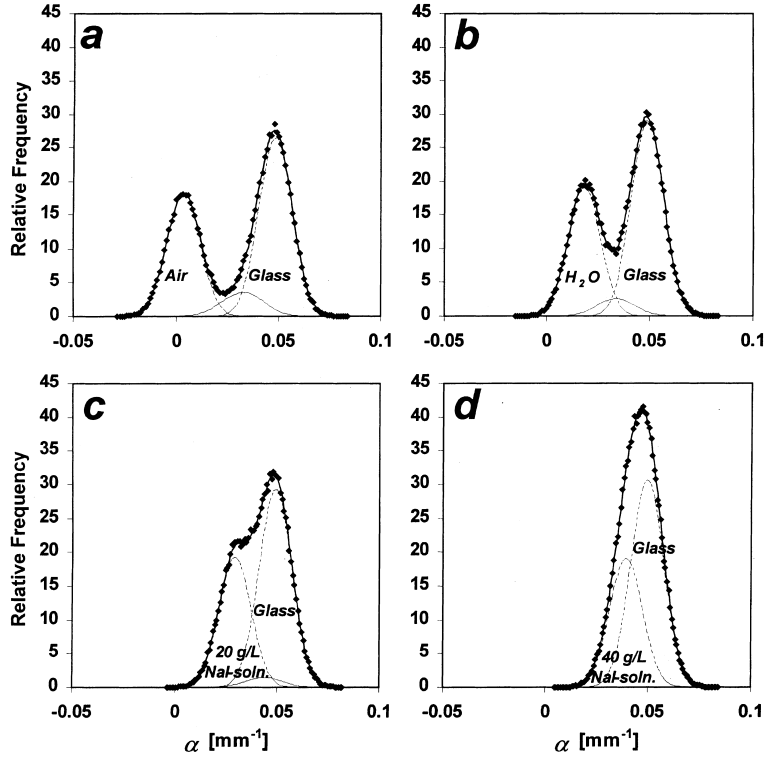

Fig. 3. Comparison of $\hat{f}$ and f for glass and air (a), glass and water (b), glass and 20-g/l NaI solution (c), and glass and 40-g/l NaI solution (d). Legend is the same as for Fig. 2.

compares the fitting results for the four remaining systems. Definition of lines and symbols is identical to Fig. 2.

Assuming that the phase interface in each data set was again blurred over approximately three voxel lengths in the normal direction, the theoretical ϕ_M-value was 0.106. However, the fraction of intermediate α-values can be expected to be increasingly masked by the noise in the pure-phase voxels as the difference between α_A and α_B decreases (a virtual one-phase system with ϕ_M equal to zero occurs if α_A and α_B are identical). Indeed, considering the fluid phases air, water, and 20-g/l NaI solution, successively smaller values of ϕ_M were estimated by the fitting procedure for a decreasing difference between α_A and α_B (Table 2 and Fig. 3). Thus a match between optimized and theoretical ϕ_M-values should only be expected if the difference between α_A and α_B is large enough, relative to σ, to provide nearly complete separation between $\theta_A f_A$ and $\theta_B f_B$, as was the case for the two glass–air systems considered (Figs. 2 and 3(a)). Prediction of θ_A was much less affected by the α-separation, suggesting robustness of the proposed procedure.

If $\phi_A f_A$ and $\phi_B f_B$ overlap to such a degree that their sum forms a single peak, it is likely that insufficient information is contained in the shape $\hat{f}(\alpha)$ to fit seven parameters, and $(\phi_A + \phi_B)$ should be fixed at unity to ensure meaningful results (thus forcing ϕ_M equal to zero and making the fitted ϕ_A-value numerically equal to θ_A). This was done in the case of the 40-g/l solution. As γ_A and γ_B can then be fixed at arbitrary values, the number of fitting parameters is reduced to four (α_A, α_B, σ, and ϕ_A), which greatly decreases the likelihood of multiple optima. If ϕ_M-values close to zero are obtained, fixing $(\phi_A + \phi_B)$ at unity during the optimization may be advantageous even if $\phi_A f_A$ and $\phi_B f_B$ do not add up to a single peak. As a test, this option was used with the 20–g/l solution, resulting in an estimated θ_A-value of 0.392.

There is excellent agreement between $\hat{f}$ and f in all cases. All estimated θ_A-values were within approximately two volume percent of the respective theoretical value. Any beam-hardening effects on the α-distribution appear to be well accounted for by the parametric model. Moreover, the results in Table 2 and Fig. 3(c) and (d) show that the proposed procedure can be applied even if there is considerable overlap between $\phi_A f_A$ and $\phi_B f_B$.

3.2 Estimation of bead-pack porosity

The proposed method was applied to determine the size of a representative elementary volume[2] (REV) for the porosity. A random pack of uniform glass beads in a vertical Plexiglas cylinder of 4.76 mm inner diameter was scanned using the previously described CT equipment. The bead diameter d_p was 0.5 mm and voxel dimensions were (18.4 μm)^3. The scanned domain included the complete object cross section over a vertical range of 3.827 mm. From the original α-set, increasingly bigger sample cubes D were extracted, all centered at the same location on the vertical cylinder axis, beginning with $8 \times 8 \times 8$ voxels and incrementing the cube side length L by 4 voxel lengths (0.0736 mm) at each step. The individual porosity (θ_A) values for all sample cubes were obtained by applying the proposed procedure to the extracted α-set of the respective sample. The maximum possible sample size had to be chosen so as to ensure exclusion of the region of higher porosity due to the presence of the cylinder wall. That size was (2.797 mm)^3, or 152^3 voxels. Two sets of $\theta_A(L)$-values were obtained, one with the sample centered in the glass phase, the other with the sample centered in the air phase. Both curves are plotted in Fig. 4. The plot suggests a REV size L/d_p of approximately 5.15. At this point the curves begin to coincide, indicating that for samples of at least this size the porosity is independent of the sample location[12]. The estimated porosity was 0.384. Fig. 5 shows the REV cube intersecting two perpendicular vertical cross sections through the original domain. Blurred voxels at the glass–air interface and the presence of noise throughout the data set are visible in the cross-sectional planes.

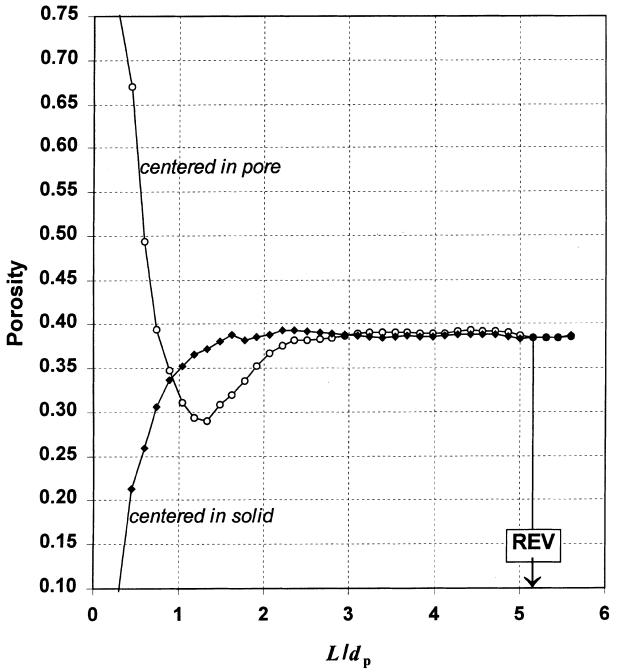

Fig. 4. Estimated porosity for a cubic domain of increasing size within a glass-bead pack, centered either within the air or the glass phase. Cube side length is expressed as multiple of the bead diameter d_p (0.5 mm).

The effect of beam hardening, inevitable with polychromatic radiation, can be clearly seen in Fig. 6 where optimized α_B-values (glass phase) are plotted as a function of L (air-phase α-values were too small to be noticeably affected). Since the center of D remains fixed at

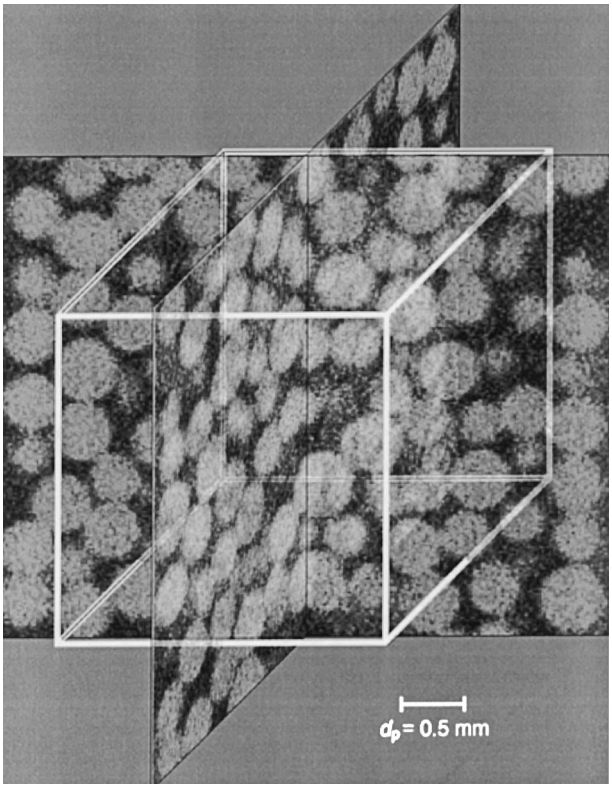

Fig. 5. Two vertical cross sections of glass-bead pack with REV of 140 voxels (2.576 mm) side length. Pore space is occupied by air. Gray scale maps α-values between -0.01 mm^{-1} (black) and 0.07 mm^{-1} (white). Bead diameter is 0.5 mm.

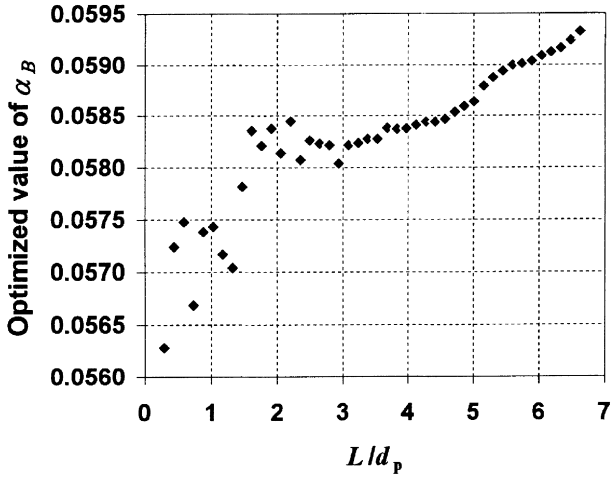

Fig. 6. Optimized value for parameter α_B as a function of domain size. The center of the domain is fixed at a point on the vertical object axis. Side length of cubic domain is expressed as multiple of the bead diameter d_p (0.5 mm).

the same point on the vertical object axis, each increase in the size of D adds voxels of increasing distance from the center. Due to beam hardening, a general increase in the average pure-phase values α_A and α_B can thus be expected with growing D. The potential for error in predicting $\theta_A(L)$ using a fixed α_B for all L is obvious from Fig. 6 and emphasizes the need to obtain the respective values for α_A and α_B from each α-set itself, as proposed here. For example, in this case a 0.003-mm^{-1} error in α_B would result in an additional four-volume-percent error in θ_A.

Lacking a true independent measure for the porosity within the considered bead pack (i.e., excluding the wall effect), confidence in the predicted porosity could be increased by its estimation from a second scan with pore air displaced by water. A sample cube corresponding in size to the previously identified REV was extracted from the water/glass α-set. The θ_A-value of 0.376 obtained using the proposed procedure was within less than one volume percent of the value estimated for the dry sample.

4 SUMMARY

A method is described to determine the phase volume fractions in two-phase systems in general, with particular applicability to the measurement of porosity in porous media. To test the method, it was applied to several two-phase systems with known volume fractions and for large and small differences between α_A and α_B. Accuracy for the considered cases was found to be approximately 2 vol% or better, including a system with only about one standard deviation difference between the mean phase α-values. Application of the method to determine the size of the representative elementary volume for porosity in a random pack of uniform glass beads was demonstrated. The value obtained for the side length of the REV was approximately 5.15 times the bead diameter.

Repeated optimization with different initial estimates for the fitting parameters is recommended to increase the likelihood of identifying the global best fit for the model PDF. If there is significant overlap between the α-distributions of both phases, the number of fitting parameters can be reduced from seven to four. Within the framework of stated assumptions, and given sufficient difference between α_A and α_B relative to σ, the method is applicable to any two-phase system of arbitrary complexity. A possible limitation could arise from the unimodal definition of $f^*_M(\alpha)$, because a more complex distribution of intermediate α-values, while not apparent for any of the considered cases, is conceivable in principle.

ACKNOWLEDGEMENTS

We are grateful to John Steude and Brett Simon of Scientific Measurement Systems, Austin, TX, and to Patrick Roberson and Dan Schneberk of the Nondestructive Evaluation Division at Lawrence Livermore National Laboratory for their valuable support and assistance. Research was supported in part by USDA NRI Proposal No. 95-37107-1602.

APPENDIX A

It is possible that n is too small to obtain a meaningful histogram due to the resulting large class size. An alternative for such cases is to fit the cumulative distribution function,

$$F(\alpha) = \int_{-\infty}^{\infty} f(\xi)\, \mathrm{d}\xi$$

to the estimated cumulative distribution $\hat{F}(\alpha)$. The cumulative distribution is given by

$$F = \phi_A F_A + \phi_B F_B + \phi_M F_M,$$

where

$$F_k = \frac{1}{2}\mathrm{erf}\left[\frac{\alpha - \alpha_k}{\sigma\sqrt{2}}\right] + \frac{1}{2}, \quad k = A, B$$

and

$$F_M \equiv \begin{cases} 0, & \alpha < \alpha_A, \\ \dfrac{\int_{\alpha_A}^{\alpha} (h*G)(\xi)\, \mathrm{d}\xi}{\int_{\alpha_A}^{\alpha_B} (\xi-\alpha_A)^{\gamma_A}(\alpha_B-\xi)^{\gamma_B}\, \mathrm{d}\xi}, & \alpha_A \leqslant \alpha \leqslant \alpha_B, \\ 1, & \alpha_B < \alpha \end{cases}$$

with

$$h(\xi) = (\xi - \alpha_A)^{\gamma_A}(\alpha_B - \xi)^{\gamma_B}.$$

The function F_M is evaluated numerically.

To obtain $\hat{F}(\alpha)$ the members of $\boldsymbol{\alpha}$ are first sorted in ascending order. This requirement, in fact, limits the applicability of this alternative method to 'small' values of n, i.e., those that are practically manageable by a sorting algorithm on the available hardware. Each $\hat{F}(\alpha_i)$ is assigned a value of $n^{-1}(i - 0.5)$, where i is the index for the ordered α-sequence starting with $i = 1$ for the smallest α-value. The discretization and lumping associated with histogram classes are thus avoided. In three tests with n equal to 77,440, θ_A-predictions deviated at most 0.1 volume percent from those obtained by fitting the PDF.

REFERENCES

1. Anderson, S.H., Gantzer, C.J., Boone, J.M. and Tully, R. J. Rapid nondestructive bulk density and soil-water content determination by computed tomography. *Soil Sc. Soc. Am. J.*, 1988, **52**, 35–40.
2. Bear, J. *Dynamics of Fluids in Porous Media*. Elsevier, Amsterdam, 1972.
3. Brown, G.O., Stone, M.L. and Gazin, J.E. Accuracy of gamma ray computed tomography in porous media. *Water Resources Res.*, 1993, **29**, 479–486.
4. Clausnitzer, V., Hopmans, J.W. Nonlinear parameter estimation: LM-OPT. General-purpose optimization code based on the Levenberg-Marquardt algorithm, Version 1.0 for UNIX. Land, Air and Water Resources Paper 100032, University of California, Davis, 1995.
5. Dyakowski, T. Process tomography applied to multi-phase flow measurement. *Measurement Sci. Tech.*, 1996, **7**, 343–353.
6. Greiner, A., Schreiber, W., Brix, G. and Kinzelbach, W. Magnetic resonance imaging of paramagnetic tracers in porous media: Quantification of flow and transport parameters. *Water Resources Res.*, (1997) **33** 1461–1473.
7. Harvel G.D., Hori, K., Kawanishi, K. and Chang, J.S. Real-time cross-sectional averaged void fraction measurements in vertical annulus gas-liquid two-phase flow by neutron radiography and X-ray tomography techniques. *Nucl. Instr. and Meth. A*, 1996, **371**, 544–552.
8. Hopmans, J.W., Cislerova, M. and Vogel, T. X-ray tomography of soil properties. In *Tomography of soil-water-root processes*. Special Publication 36, Soil Science Society of America, 1994, pp. 17–28.
9. Hopmans, J.W., Vogel, T. and Koblik, P.D. X-ray tomography of soil water distribution in one-step outflow experiments. *Soil Sci. Soc. Am. J.*, 1992, **56**, 355–362.
10. Hsieh, H.T., Brown, G.O. and Stone, M.L. Measurement of porous media component content and heterogeneity using gamma ray tomography. *Water Resources Res.*, 1998, **34**, 365–372.
11. Klobes, P., Riesemeier, H., Meyer, K., Goebbels, J. and Hellmuth, K.H. Rock porosity determination by combination of X-ray computerized tomography with mercury porosimetry. *Fresenius J. Anal. Chem.*, 1997, **357**, 543–547.
12. Kutilek, M. and Nielsen, D.R., *Soil Hydrology*. Catena Verlag, 1994, p. 16.
13. Rowland, S.W. Computer implementation of image reconstruction formulas. In *Image reconstruction from projections. Topics in Applied Physics 32*, ed, G.T. Herman, Springer, Berlin, 1979.
14. Steude, J.S., Sullivan, C.P., Chaney, R.C., McKee, M. and O'Shea, L.E. Tracer experiments in saturated sand by computed tomography and inductively coupled plasma, In: *Physico-chemical aspects of soil and related materials*, eds, K.B. Hoddinott and R.O. Lamb, Am. Soc. for Testing and Materials STP 1095, Philadelphia, 1990, pp. 171–184.
15. Vinegar, H.J. and Wellington, S.L., Tomographic imaging of three-phase flow experiments. *Rev. Sci. Instr.,* 1987, **58**, 96–107.